The Planetary Science Journal, 4:86 (15pp), 2023 May https://doi.org/10.3847/PSJ/acd056

New Compound and Hybrid Binding Energy Sputter Model for Modeling Purposes in Agreement with Experimental Data

Noah Jäggi[1], Andreas Mutzke[2], Herbert Biber[3], Johannes Brötzner[3], Paul Stefan Szabo[4], Friedrich Aumayr[3], Peter Wurz[1], and André Galli[1]
[1] Physikalisches Institut, University of Bern, Sidlerstrasse 5, CH-3012 Bern, Switzerland; noah.jaeggi@unibe.ch
[2] Max Planck Institute for Plasma Physics (IPP), D-17491 Greifswald, Germany
[3] Institute of Applied Physics, TU Wien, Wiedner Hauptstraße 8-10/E134, A-1040 Vienna, Austria
[4] Space Sciences Laboratory, University of California, 7 Gauss Way, Berkeley, CA 94720, USA
Received 2023 January 24; revised 2023 April 13; accepted 2023 April 24; published 2023 May 12

Abstract

Rocky planets and moons experiencing solar wind sputtering are continuously supplying their enveloping exosphere with ejected neutral atoms. To understand the quantity and properties of the ejecta, well-established binary collision approximation Monte Carlo codes like TRIM with default settings are used predominantly. Improved models such as SDTrimSP have come forward, and together with new experimental data, the underlying assumptions have been challenged. We introduce a hybrid model, combining the previous surface binding approach with a new bulk binding model akin to Hofsäss & Stegmaier. In addition, we expand the model implementation by distinguishing between free and bound components sourced from mineral compounds such as oxides or sulfides. The use of oxides and sulfides also enables the correct setting of the mass densities of minerals, which was previously limited to the manual setting of individual atomic densities of elements. All of the energies and densities used are thereby based on tabulated data, so that only minimal user input and no fitting of parameters are required. We found unprecedented agreement between the newly implemented hybrid model and previously published sputter yields for incidence angles up to 45° from surface normal. Good agreement is found for the angular distribution of mass sputtered from enstatite $MgSiO_3$ compared to the latest experimental data. Energy distributions recreate trends of experimental data of oxidized metals. Similar trends are to be expected from future mineral experimental data. The model thus serves its purpose of widespread applicability and ease of use for modelers of rocky body exospheres.

Unified Astronomy Thesaurus concepts: Solar wind (1534); Exosphere (499); Mercury (planet) (1024); The Moon (1692)

1. Introduction

In recent years there were several efforts to better constrain the erosion of rocky planetary bodies exposed to highly energetic solar wind ions. This includes investigating the effect of surface roughness (Biber et al. 2022) and porosity (Szabo et al. 2022b), performing ion irradiation experiments with mass yield measurements (e.g., Hijazi et al. 2017; Szabo et al. 2018, 2020a; Biber et al. 2022), and introducing a new surface and bulk binding energy (BBE) model from theory (Hofsäss & Stegmaier 2022; Morrissey et al. 2022). In this work, we discuss the parameter of density and its inclusion in SDTrimSP (Mutzke et al. 2019), as well as a new hybrid binding energy model that reliably recreates experimental sputter yields completely without the requirement to adjust input parameters. The new approach will be a valuable tool for modeling the ion sputtering contribution to exospheres (i.e., Pfleger et al. 2015; Suzuki et al. 2020; Kazakov et al. 2022; Killen et al. 2022).

1.1. Space Weathering of Exposed Rocky Surfaces

Exposed bodies in space are subject to solar wind irradiation. The main constituents of solar wind, H^+ and He^{2+}, thereby bear kinetic energies of approximately 1 keV amu^{-1}—equivalent to about 440 km s^{-1} (Wurz 2005; Gershman et al. 2012; Baker et al. 2013; Winslow et al. 2013). When hitting a surface, most ions are neutralized and enter the sample, with some fraction being reflected as either neutrals or even ions (Lue et al. 2011; Vorburger et al. 2013). The ions entering the sample initiate a cascade of collisions with a chance to eject particles from the near surface at suprathermal energies. This process is responsible for altering the surface composition and creating lattice defects, which leads to amorphization (Betz & Wien 1994; Loeffler et al. 2009; Dukes et al. 2011; Domingue et al. 2014).

Ion sputtering releases atoms from the surface having typical velocities that are significantly lower than the impinging ions (e.g., Thompson 1968), but large enough to form an extended exosphere with a significant fraction of atoms exceeding the escape velocity of any small body, including the Moon (2.4 km s^{-1}) and Mercury (4.3 km s^{-1}) (e.g., Wurz et al. 2007, 2010). Such exospheres allow for ground-based observatories and space probe missions such as LADEE and LRO at the Moon (Paige et al. 2010; Elphic et al. 2014) and MESSENGER (Solomon et al. 2001; McNutt et al. 2018) or the future BepiColombo (Benkhoff et al. 2010; Milillo et al. 2020; Orsini et al. 2021) at Mercury to detect them. These observations were used early on to self-consistently model Mercury's surface composition based on the four expected major processes contributing to the exosphere: solar wind ion sputtering, micrometeroid impact vaporization, photon-stimulated desorption, and thermal desorption (Madey et al. 2002;

Mura et al. 2009; Wurz et al. 2010; Gamborino & Wurz 2018; Wurz et al. 2022).

An important piece of information that is necessary to distinguish the exospheric species sourced from the surface is the process-specific energy distribution of the ejected material. For example, solar wind ion sputtering and micrometeroid impact vaporization compete in supplying Mercury's exospheric high-energy particle population with refractory species (e.g., Ca and Mg), while photon-stimulated desorption dominates the supply of energetic volatile and moderately volatile species (i.e., Na, K, and S; Mangano et al. 2007; Cassidy et al. 2015; Schaible et al. 2020; Grava et al. 2021; Janches et al. 2021). In the same way that fluxes, or precipitation rates, of the particles causing these processes are still in the process of being better constrained (i.e., proton precipitation for solar wind sputtering at Mercury's cusps in Fatemi et al. 2020; Glass et al. 2022; Raines et al. 2022), the understanding of the underlying physics is still a work in progress. At the Moon, precipitation rates seem comparably trivial to compute, but the Moon traveling through Earth's magnetotail and localized crustal fields add complexity to the system (e.g., Lue et al. 2011; Poppe et al. 2018; Nénon & Poppe 2020).

1.2. Sputter Models

To efficiently model ion-induced sputtering, binary collision approximation (BCA) models are used. The BCA codes track particles as they travel through the sample and cause recoils, which are in turn tracked throughout the sample. There are many different models available; however, we will focus on the results of the Monte Carlo−based, most widely used TRIM code (Biersack & Haggmark 1980) in the SRIM package (Ziegler et al. 2010) as well as its successor SDTrimSP (Mutzke et al. 2019), a combined and improved version of the static TRIM.SP (Biersack & Eckstein 1984), and the dynamic TRYDIN (Möller & Eckstein 1984).

TRIM has been shown to overestimate the sputter yield compared to experimental yields for minerals (Szabo et al. 2018). Exosphere modelers need more accurate inputs that are in line with the latest understanding of sputtering. There have been several suggestions on how to best recreate experimental data. Here are the major contributions that set the expectations and limitations of the current state-of-the-art sputter modeling:

1. Schaible et al. (2017) varied O-binding energies to better fit early experimental data for sputtering of Al_2O_3 and SiO_2 (Ken Knight & Wehner 1967; Roth et al. 1979). Increasing the O-binding energy decreases the O yield, but not enough to significantly improve the agreement.
2. Szabo et al. (2020a) suggested that the best agreement between the mass yield of an irradiated sample and SDTrimSP is obtained by (a) adjusting atomic densities to obtain an appropriate sample density, (b) adjusting the surface binding energy (SBE) of O to 6.5 eV, and (c) setting the SBEs of each element to the averaged SBE of all elements in the sample, resulting in an SBE that is highly dependent on the O concentration in the sample (Appendix). Although we found these parameters to work reasonably well for all kinds of silicates, the universality of these modifications is questionable.
3. Morrissey et al. (2022) determined SBEs using molecular dynamics (MD) and suggest lower sputter yield across all surface species due to an increase in the single component's binding energies. However, the restricted availability of species-specific SBEs prevents the applicability of the results on a broad range of minerals. This is also caused by the limited availability of interatomic potentials for each mineral system of interest.
4. Hofsäss & Stegmaier (2022) proposed completely neglecting SBEs and instead using only BBEs from tabulated data. This way, particles leaving the sample do not have to overcome a surface potential and instead lose energy with each recoil. Although they solely use tabulated data to set the BBE and propose a sound physical constraint on the cutoff energy for the tracing of the particles, they are still required to make use of an undisclosed level of implantation to find good agreement with experimental data.
5. Biber et al. (2022) used the in-house-built ray-tracing code SPRAY (Cupak et al. 2021) with data from SDTrimSP and atomic force microscope images to discuss the effect of surface roughness on the sputter yield of a powder pellet and a flat, glassy thin film. They found that a rough pressed pellet surface reduces the yield, especially at shallow incident angles (above 45° relative to surface normal). The cause of this reduced yield was related to surface roughness leading to shallower local incident angles, shadowing, and redeposition of material. For a detailed overview of rough surface sputter models see Küstner et al. (1998) and Arredondo et al. (2019).

All these models require varying degrees of adjustments of parameters when it comes to density, binding energies, cutoff energies, or roughness. To adequately describe the sputtering process on realistic surfaces, roughness has to be taken into account. This effect is not considered in this work, as we focus on the fundamental sputter physics within the sample, which is agnostic to properties affecting trajectories of impinging ions and ejecta. For this reason, we compare our results to experimental thin-film data, which are considered to be flat surfaces (Biber et al. 2022). We propose a new compound model for obtaining a realistic initial mineral density, as well as a hybrid binding energy model to obtain increased binding energies based on tabulated data that can recreate experimental results.

2. Methods of Computation

2.1. Model Parameters

Angular-dependent sputter yields for various different models were calculated with SDTrimSP to compare with a wide range of experimental data. To obtain good statistics in SDTrimSP, we modeled between 7.7×10^6 and 31×10^6 impactors for each of 19 incident angles between 0° and 89° relative to the surface normal (Mutzke et al. 2019). The step size was set to gradually decrease from an initial 10° for incidence close to the surface normal to 2° for incidence angles 80°–88°. We collected the information of up to 10^6 recoils leaving the sample and performed statistics based on the last 10^5 recoils. The data contain the species name, end energy, azimuth angle, and zenith angle. The fits of the data shown in the figures throughout this manuscript are described in Section 2.5. The inelastic loss model seven (inel = 7) is used in all SDTrimSP calculations, which determines the inelastic

Table 1
Major Rock-forming Minerals Required to Represent an Unknown Planetary Surface, Consisting of Volcanic Minerals

Group	Mineral	Formula	ρ_{ref}		$\rho_{compounds}$		$\Delta\mu_{compounds}$	ρ_{atomic}		$\Delta\mu_{atomic}$
			(g cm^{-3})	(atoms Å^{-3})	(g cm^{-3})	(atoms Å^{-3})	(unit of unity)	(g cm^{-3})	(atoms Å^{-3})	(unit of unity)
Plagioclase	Orthoclase	$KAlSi_3O_8$	2.56	0.0723	2.67	0.0754	−1%	1.36	0.0384	23%
	Albite	$NaAlSi_3O_8$	2.62	0.0786	2.70	0.0808	−1%	1.43	0.0429	22%
	Anorthite	$CaAl_2Si_2O_8$	2.73	0.0768	2.99	0.0840	−3%	1.53	0.0429	21%
	Nepheline	$NaAlSiO_4$	2.59	0.0747	2.84	0.0820	−3%	1.44	0.0414	22%
Pyroxene	Wollastonite	$CaSiO_3$	2.93	0.0760	2.91	0.0755	0%	1.45	0.0375	26%
	Diopside	$CaMgSi_2O_6$	3.40	0.0946	2.97	0.0827	5%	1.46	0.0405	33%
	Enstatite	$Mg_2Si_2O_6$	3.20	0.0960	3.05	0.0913	2%	1.47	0.0441	30%
	Ferrosillite	$Fe_2Si_2O_6$	3.95	0.0902	3.82	0.0872	1%	2.15	0.0491	22%
Olivine	Forsterite	Mg_2SiO_4	3.27	0.0980	3.21	0.0960	1%	1.46	0.0438	31%
	Fayalite	Fe_2SiO_4	4.39	0.0908	4.64	0.0900	0%	2.48	0.0512	21%
Oxides	Ilmenite	$FeTiO_3$	4.72	0.0937	4.83	0.0959	−1%	2.54	0.0504	23%
	Quartz	SiO_2	2.65	0.0797	2.65	0.0797	0%	1.51	0.0454	21%
Sulfides	Troilite	FeS	4.61	0.0632	4.61	0.0632	0%	3.89	0.0533	6%
	Niningerite	MgS	2.68	0.0573	2.68	0.0573	0%	1.91	0.0408	12%
	MnS	MnS	3.99	0.0552	3.99	0.0552	0%	3.80	0.0526	2%
	CrS	CrS	4.89	0.0701	4.89	0.0701	0%	3.70	0.0530	10%
	TiS	TiS	3.85	0.0580	3.85	0.0580	0%	3.07	0.0462	8%
	CaS	CaS	2.59	0.0432	2.59	0.0432	0%	1.74	0.0290	14%
Accessories	Spinel	$MgAl_2O_4$	3.64	0.1078	3.77	0.1115	−1%	1.58	0.0468	32%
	Chromite	$FeCr_2O_4$	4.79	0.0902	5.29	0.0996	−3%	2.88	0.0543	18%

Note. Differences in mean free path lengths ($\mu = \rho^{-1/3}$) are calculated as $\Delta\mu = \mu/\mu_{ref} - 1$. The density short forms are as follows: ρ_{ref}—mass densities and atomic densities calculated based on typical mineral densities found on webmineral (see also, e.g., Deer et al. 1992); $\rho_{compounds}$—densities calculated based on tabulated oxide and sulfide data from pure compound properties; ρ_{atomic}—densities calculated based on atomic data included in tables of SDTrimSP that are based on monatomic solids.

loss in the sample based on the Lindhard–Scharff stopping power model (Lindhard & Scharff 1961) unless there are corrections available (e.g., tables for H and He in Ziegler & Biersack 1985). For a detailed description of SDTrimSP, we encourage the reader to look into the accompanying literature (e.g., Mutzke et al. 2019).

The surface composition of irradiated samples show a clear fluence dependence until an equilibrium is reached. This was shown by Baretzky et al. (1992) for the oxide Ta_2O_5 and by Szabo et al. (2020b) in the form of the fluence dependence of experimental sputter data of minerals. Furthermore, the experimental sputter yields were best recreated using the dynamic mode of SDTrimSP (Szabo et al. 2020b). For this reason, all computations in this manuscript were performed in dynamic mode of SDTrimSP, and the results are for ejecta from a surface in equilibrium with the impinging ions. For irradiation with He, the fluence was set to 750 atoms Å^{-3}, whereas H irradiation required fluences of up to 3000 atoms Å^{-3} (or 3×10^{19} atoms cm^{-3}) at normal incidence in some models. The dynamic mode allows the sample to change with the ion fluence and best simulates the sample composition reaching an equilibrium with the solar wind ions, reproducing the fluence dependence of the experimental sputter yields. In detail, samples in SDTrimSP have an infinite lateral extent with a finite number of layers vertically. In our case, all layers have the same composition set initially and a thickness of 10 Å. After each fluence step, composed of about 10^5 impactors, the layers within the sample are updated according to the components that were either lost or gained within the last step.

Direct comparisons between SRIM and SDTrimSP calculations were performed for mass yield (amu ion^{-1}). In SRIM (Ziegler et al. 2010) we modeled 10^5 impinging H and He ions for static sputter yield results to obtain good statistics. We used the "Monolayer Collision Steps/Surface Sputtering" damage model. The mineral density was set to its default density, as calculated by SRIM from the atomic density value of each element component (comparable to ρ_{atomic} from tabulated data in SDTrimSP given in Table 1).

We will now introduce a few select parameter settings that are required to model sputtering of minerals. These comprise the dynamic mode of SDTrimSP, the different ways of introducing binding energies, including our new addition, and a new way for correcting sample density.

2.2. Binding Energy

The efficiency at which particles can be removed from a surface, the sputter yield, is in one part a function of the total binding energy of the system. The two common binding energies provided to a BCA model are the SBE and the BBE. The former is in the shape of a surface potential that has to be overcome to leave the sample. The latter is an energy that is subtracted from each recoil and simulates the interaction between neighboring atoms in the otherwise mineral-lattice-agnostic model that is SDTrimSP. It is possible to obtain a constant yield while keeping the sum of the binding energies constant (Möller & Posselt 2001). We now quickly introduce three different binding energy models, two of which are already established (pure SBE or BBE models) and one model that combines the two (SBE + BBE). The models are summarized in Table 2.

Table 2
The Different Energy and Density Models and Their Parameters

	SDTrimSP Model Presets					Manually Set Models	
	SB	SB-C	BB	BB-C	HB-C	BB_0[a]	HB[a]
SBE	ΔH_{sub}	ΔH_{sub}	0	0	ΔH_{sub}	0	ΔH_{sub}
BBE_f[b]	0	0	ΔH_{sub}	0	0	ΔH_{sub} + CBE	CBE
BBE_b[b]	⋯	0	⋯	ΔH_{sub} + CBE	CBE	⋯	⋯
ρ_f	atomic	atomic	atomic	atomic	atomic	atomic	atomic
ρ_b	⋯	compound	⋯	compound	compound	⋯	⋯
E_{cutoff}	$<\Delta H_{sub}$	$<\Delta H_{sub}$	$\Delta H_{sub}/3$	$\Delta H_{sub}/3$	$<\Delta H_{sub}$	$\Delta H_{sub}/3$	$<\Delta H_{sub}$
isbv	1	1	8	8	4	1	1

Notes. Short forms: SBE—surface binding energy; BBE—bulk binding energy; f—"free," unbound atom; b—compound-bound atom; CBE—chemical binding energy: $\Delta H_f/(m+n)$, where m and n are the number of cations and anions in a compound, respectively; E_{cutoff}—cutoff energy; ΔH_{sub}—enthalpy of sublimation; ΔH_f—enthalpy of formation of binary compound; isbv—model number in SDTrimSP input files.
[a] Each component is considered unbound with regard to its density and bound with regard to the BBE (CBE assigned). The BB_0 model is the original Hofsäss & Stegmaier (2022) model. The HB model is only used to demonstrate the effect of density independent of the hybrid binding energy model.
[b] For O, ΔH_{sub} is neglected and only CBE is used as a BBE, if any.

2.2.1. SB: Surface Binding Model

The surface binding (SB) model is the default calculation model for TRIM and SDTrimSP. In this approach, a particle may leave the sample only if its kinetic energy exceeds the SBE. Energy loss within the sample occurs through elastic energy transfer during collisions and inelastic electronic losses.

Although the SBE is an energy determined by the attractive forces of neighboring atoms (Sigmund 1969; Gades & Urbassek 1992), it is common practice to approximate the SBE as the atomic enthalpy of sublimation (ΔH_S). The exception are gases where the SBEs are based on the enthalpy of dissociation. For example, pure O does not form a solid, and therefore the dissociation enthalpy of oxygen $\Delta H_{diss}(O_2)$ is used instead of the sublimation enthalpy. Hobler and Morrissey showed for Si and Na that the atomic enthalpy of sublimation can severely underestimate the energy necessary to remove an atom from their crystalline structure (Hobler 2013; Morrissey et al. 2022). This was determined by the means of MD calculations, which take into account the bonds between atoms. The results have so far only been tentatively confirmed for nepheline ($NaAlSiO_4$; Martinez et al. 2017) where the sputtered secondary Na^+ ions express a peak in their energy distribution around 2.4 eV, which was attributed to an SBE of Na of 4.8 eV (Morrissey et al. 2022). This exceeds the tabulated value of 1.1 eV by a factor of 4.3. Interestingly, the secondary K^+ ion results of Martinez et al. (2017) would suggest K SBEs of 4 eV, also exceeding the tabulated value of 0.93 eV by the same factor. Morrissey et al. (2022) also found that within plagioclase—the primary Na-bearing mineral on a planetary surface—the SBE is increased to 7.9 eV in the Na end member albite ($NaAlSi_3O_8$), which would result in a reduction of the Na sputter yield from albite by a factor of 15. The MD results therefore show a positive correlation between SBE and Na coordination number (amount of neighboring atoms).

How the SBE of a damaged surface or, as outlined by Hofsäss & Stegmaier (2022), a nonnormal orientation of a mineral unit cell would differ from the ideal conditions chosen in MD simulations is unclear. Furthermore, the energy distributions of secondary ions do not necessarily represent their neutral counterparts, as neutralization of ejected particles is energy dependent, which can cause a significant offset of the ion distribution toward lower energies (Benninghoven et al. 1987; Van der Heide 2014). Another example that adds to the uncertainty of the link between neutral and ion energy distributions is from Betz (1987), who showed that ground-state Ba sputtered from a continuously oxidized Ba surface coincides with metastable Ba (originating from the decay of short-lived, excited-state Ba) and Ba ions from a nonoxidized surface. Ground-state Ba from a nonoxidized surface expresses a significantly lower peak energy that can be related to the ΔH_S. The energy distributions of ions, metastable atoms, and ground-state atoms coincide with each other and exceed ΔH_S. The larger energy of ions and metastable atoms are interpreted to be caused by matrix-dependent ionization processes (e.g., Dukes & Baragiola 2015), whereas the increased energy of the sputtered ground-state atoms from an oxidized sample is so far not well understood and depends on the procedure including a single initial oxidation or, as in Betz (1987), a continuous oxidation. What is certain is that the displacement and removal of atoms that would lead to changes in bonds within the sample alters coordination numbers and therefore the binding energy that has to be overcome for their removal. The interatomic potentials between the atoms in the sample would end up far from equilibrium, which is commonly neglected in MD simulations owing to computational load (Behrisch & Eckstein 2007). Lastly, Hobler (2013) compared MD and BCA results and concluded that the enthalpy of sublimation approximation works well in BCA to reproduce experimental data, even when the crystalline structure of the mineral is not taken into account. The reasoning behind this is that in MD simulations an increase of yield is tied to an increase in defect creation, which ultimately negates the effect of the higher SBEs in the MD simulation. The increased SBEs suggested by MD models are to be taken with caution, but it is established that an overall increase in energy loss within the sample is necessary to best fit experimental data.

2.2.2. BB: Bulk Binding Model

The bulk binding (BB) model was recently suggested by Hofsäss & Stegmaier (2022). It sets the SBE to zero, while setting a BBE for each component that has to be overcome for a component to be freed from their sample and that is lost during each recoil. The authors used the enthalpy of sublimation (E_s) for single-species samples (i.e., the tabulated values used as SBEs in the SB model). For binary compounds, such as oxides and sulfides in minerals, the enthalpy of formation (ΔH_f) has to

be overcome before the enthalpy of sublimation of each component, thereby increasing the energy loss in the sample (as suggested earlier by Dullni 1984).

In SDTrimSP, the implementation of the BB model is similar but slightly different. The sublimation enthalpy of species that form gases under standard conditions is neglected when determining E_{bulk} (Table 2). This is based on the assumption that, e.g., O from breaking up SiO_2 will already be in its gaseous state and thus will not be required to be sublimated, unlike Si. As an example, E_{bulk} (or BBEs) for the elements in the binary compound SiO_2 are, as implemented in SDTrimSP,

$$\begin{aligned} E_{bulk}(\mathrm{Si}) &= E_s(\mathrm{Si}) + \frac{\Delta H_f(\mathrm{SiO_2})}{m+n} \\ &= 4.664\ \mathrm{eV} + \frac{9.441\ \mathrm{eV}}{3} = 7.701\ \mathrm{eV} \\ E_{bulk}(\mathrm{O}) &= \frac{\Delta H_f(\mathrm{SiO_2})}{m+n} \\ &= \frac{9.441\ \mathrm{eV}}{3} = 3.147\ \mathrm{eV}, \end{aligned} \tag{1}$$

with m and n being the number of components Si and O in the compound (Si_mO_n). In SDTrimSP, this model is implemented as the SB model eight (isbv = 8), which is only available when using the new density model introduced in Section 2.4.2.

A side effect of setting the SBE to zero and only using a BBE is a lack of a planar attraction potential, and therefore no refraction of sputtered particles toward larger emission angles occurs (Jackson 1975; Roth et al. 1983; Gades & Urbassek 1992; Hofsäss & Stegmaier 2022). When a surface potential has to be overcome, the extent of the refraction acting on a particle leaving the surface of a sample is proportional to the ratio of the energy of the particle in relation to the potential that has to be overcome (Thompson 1968; Sigmund 1969):

$$\sin(\theta_1) = \sqrt{\frac{E_0}{E_0 - E_{sbe}}}\sin(\theta_0), \tag{2}$$

with the incident energy E_0, the SBE E_{sbe}, the angle of the atom crossing the surface barrier θ_1, and the initial incident angle of the atom θ_0. Instead, in the BB model, any released particle inside the compound can travel freely through the surface, independent of its energy.

In BCA computations, a cutoff energy (E_{cutoff}) for each species is set that determines when a recoil is considered to be "at rest" and no longer causes collisions. In the SB model, E_{cutoff} is chosen to be 0.1 eV below the lowest, nonzero E_s of all species within the sample. Choosing a lower E_{cutoff} would increase computation times owing to the impactor traveling deeper into the sample before it is considered at rest. In the context of this work, longer impactor paths are irrelevant because recoils that are below E_{cutoff} do not contribute to the sputter yield. Any recoil from within the sample needs to exceed the SBE to leave the compound with an energy E_{ejecta} of

$$E_{ejecta} = E_{recoil} - \mathrm{SBE}. \tag{3}$$

This explains why the E_{cutoff} should not be chosen to exceed the SBE of any given component. A recoil of a relatively heavy species that is too slow to overcome the SBE is still capable of causing recoils of lighter species with kinetic energies exceeding their SBE.

For the BB model, however, the BBE is subtracted at each collision, after which recoils can leave the sample without further change of their energy. This energy can therefore be arbitrarily small and has to be limited by the cutoff energy for convergence. With the cutoff, E_{ejecta} cannot be inferior to the cutoff energy E_{cutoff},

$$E_{ejecta} \geqslant E_{cutoff}. \tag{4}$$

The suggested approach by Hofsäss & Stegmaier (2022) to obtain the best results to reproduce experimental data is to set a cutoff energy (E_{cutoff}) in the BB model that lies between 1/2 and 1/8.5 of the atomic E_s (the authors thereby favor a factor of 1/3, which is also the default set for BB models in SDTrimSP). The effect of the absence of an SBE and the use of a BBE and E_{cutoff} on the energy distribution of the sputtered particles is evident, as the lower energetic tail of sputtered atoms is cut off at the given E_{cutoff}, and no Thompson distribution (Thompson 1968) is seen (Figure 1). For the example of SiO_2, we obtain

$$\begin{aligned} E_{cutoff}(\mathrm{O}) &= \frac{E_s(\mathrm{O})}{3} = 0.861\ \mathrm{eV} \\ E_{cutoff}(\mathrm{Si}) &= \frac{E_s(\mathrm{Si})}{3} = 1.555\ \mathrm{eV}. \end{aligned} \tag{5}$$

2.3. HB: New Hybrid Binding Energy Model

The planar potential on the surface is an issue, as its strength needs to exceed atomic enthalpies of sublimation to properly reproduce experimental data. The presence of such a surface potential is, however, supported by previous energy distribution measurements (Betz & Wien 1994; Samartsev & Wucher 2006; Martinez et al. 2017). Furthermore, metals covered by a layer of O_2 express energy peak broadening and a slight shift to larger energies (Dullni 1984; Wucher & Oechsner 1986, 1988). The energy distribution of the BB model is thus only fitting to sputtering of binary metal compounds where monotonously decreasing energy distributions were observed with peak energies close to zero (Szymoński 1981). In oxide-bearing minerals we would thus expect a behavior where the energy distribution is affected proportionally with the amount of available O. Neither the SB nor the BB model is capable of taking this into account, which demands a new model.

We introduce a hybrid binding energy model (HB) that uses the element enthalpy of sublimation as SBE and the enthalpy of formation for compounds as BBE. The energies thus represent a surface potential that has to be overcome and the bonds within the sample, which have to first be broken up before an atom is mobilized. The model is based purely on tabulated data, just like the BB model of Hofsäss & Stegmaier (2022) but without the need of a specific E_{cutoff} to best reproduce sputter yields and energy distributions. It therefore poses a promising alternative to the previous approaches for obtaining increased binding energies.

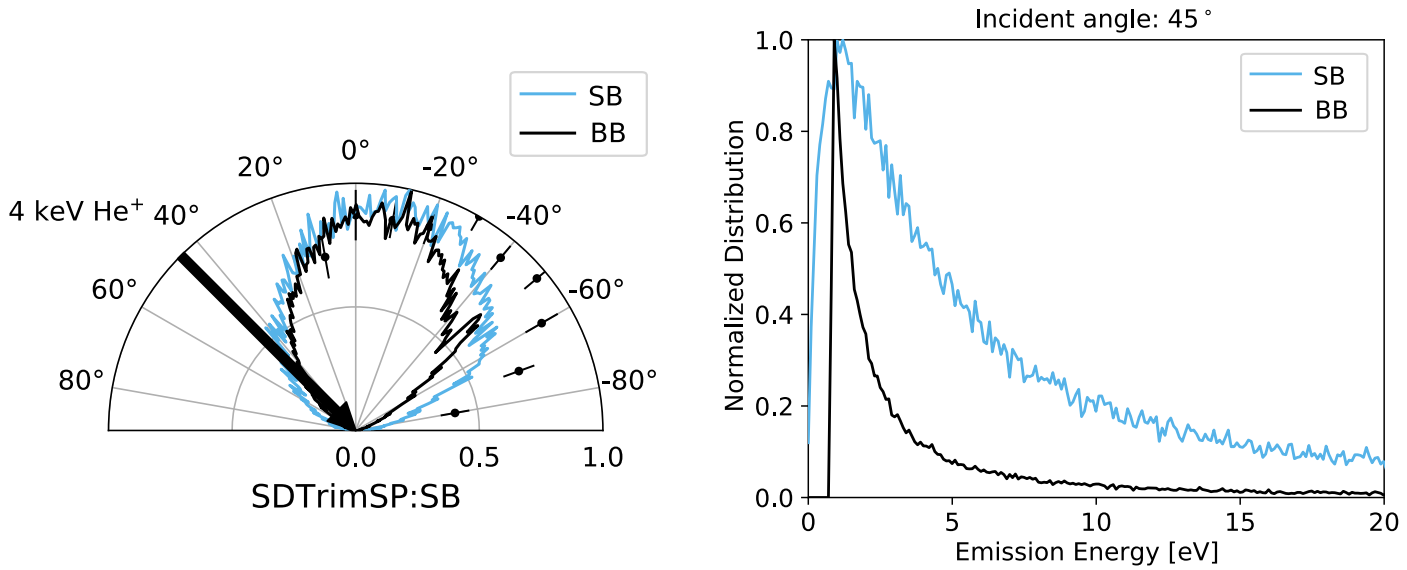

Figure 1. Model comparison for angular distributions of total sputtered mass yield (left) and energy distribution of sputtered O (right) from irradiated enstatite ($MgSiO_3$) for impinging He ions at an incident angle of 45° and energy of 4 keV. The BB model (black line) is based on the pure BBE assumption, where a lack of an SBE prevents scattering of the particles toward the surface, resulting in ejecta being preferentially emitted toward the surface normal. The energy distribution of the BB model does not express the characteristic Thompson distribution but instead shows a monotonously decreasing distribution, starting at the element-specific cutoff energy of $\Delta H_s/3$. The SB model (light-blue line) shown for comparison is calculated with an SBE instead of the BBE. The experimental data are from thin-film irradiation (Biber et al. 2022) and normalized to $y_{max} = 1$ with an error of one standard deviation.

As an example, the SBE and BBE for the binary compound SiO_2 result in

$$\begin{aligned} E_{\mathrm{surf}}(\mathrm{Si}) &= E_s(\mathrm{Si}) = 4.664\ \mathrm{eV} \\ E_{\mathrm{bulk}}(\mathrm{Si}) &= \frac{\Delta H_f(\mathrm{SiO_2})}{m+n} \\ &= \frac{9.441\ \mathrm{eV}}{3} = 3.147\ \mathrm{eV} \\ E_{\mathrm{surf}}(\mathrm{O}) &= \frac{\Delta H_{\mathrm{diss}}(\mathrm{O_2})}{2} = 2.582\ \mathrm{eV} \\ E_{\mathrm{bulk}}(\mathrm{O}) &= \frac{\Delta H_f(\mathrm{SiO_2})}{m+n} \\ &= \frac{9.441\ \mathrm{eV}}{3} = 3.147\ \mathrm{eV}. \end{aligned} \tag{6}$$

The BBEs that are determined from binary compounds only hold as long as we assume that each element remains bound over the course of irradiation. This is naturally not the case and led in consequence to the implementation of a more sophisticated compound model.

2.4. New Compound Model

We propose a simple model for sample compositions that serves two purposes. It allows discrimination between chemically bound atoms and "free" atoms (not chemically bound), and it allows us to use data of compounds (i.e., oxides and sulfides) to adequately approximate realistic mass densities of minerals. The simulation names using this compound model to differentiate between bound and unbound atoms, as well as density, are labeled by "-C" (HB-C, for the combination of compound and hybrid model; Table 2).

2.4.1. Discriminate between Bound and Free Atoms

Instead of using single atoms, the starting condition considers each atom to be bound to its respective compound —for example, Si and O are bound in SiO_2. If a recoil occurs with sufficient energy to overcome the BBE, the bound atom is unbound. The atomic species produced by breaking up compounds no longer have a chemical binding energy (BBE = 0; Table 2). If the remaining energy after the collision is large enough, the target atom can move through the sample. The atom then either comes to a halt and attempts to re-form a bond or is ejected. To prevent a major accumulation of atomic species, free atoms react to form the initially set compounds again whenever possible. In the current SDTrimSP implementation, the compound with the highest formation enthalpy is prioritized to re-form given the available O. This has the desired effect that oxygen is unlikely to ever exist as a free atom. In SDTrimSP, the compound hybrid model is implemented as the SB model four (isbv = 4). In the noncompound models BB and HB, each component within the sample has a fixed BBE owing to the atomic model not being capable of differentiating bound from free components (Table 2). They therefore do not behave identically to their compound counterparts (BB-C and HB-C), which causes major differences especially between the HB and HB-C energy and angular distributions (Section 3).

2.4.2. Set Atomic Density with Compounds

It was found that the best-fitting models to sputter yields for mineral require not only an increase in binding energy (as already hinted at in, e.g., Dullni 1984) but also an accurate model that reflects realistic material properties, including the atomic density (e.g., Szabo et al. 2020a). The default way of determining densities in SDTrimSP and TRIM is by using tabulated data of atomic species. In Szabo et al. (2020a), the authors follow Möller & Posselt (2001) and calculate a density for wollastonite ($CaSiO_3$) based on tabulated atomic densities, which results in 0.0376 atoms $Å^{-3}$. Increasing the density of oxygen ρ_O to 0.7 atoms $Å^{-3}$ (from an initial 0.04 $Å^{-3}$) leads to a bulk density more akin to the wollastonite density of

0.07412 atoms $Å^{-3}$, corresponding to 2.86 g cm^{-3}. This value for ρ_O exceeds the typical atomic density by over an order of magnitude. Therefore, in dynamical modeling removal of oxygen causes disproportionate changes to the surface density of the compound compared to removing any other element. To prevent this, we propose calculating mineral densities based on the tabulated atomic densities of compounds, which are simplified building blocks of minerals.

In SDTrimSP, the density of each layer of the sample is calculated based on the density of its components with

$$\rho = \left(\sum_{1}^{n} \frac{X_n}{\rho_n} \right)^{-1}, \tag{7}$$

where ρ is the density of the sample, X_n the atomic fraction, and ρ_n the density of the nth component.

The atomic densities and atomic fractions define the bulk density, and therefore the mean free path between two atoms in the sample. The mean free path μ is formulated in SDTrimSP as

$$\mu = \rho^{-1/3}. \tag{8}$$

In BCA simulations such as SDTrimSP, an ion traveling through the sample will gradually lose its energy through nuclear and electronic interactions, which influence its motion (e.g., Eckstein 1991). After the impinging ion has traveled the distance μ, a collision occurs (Eckstein 1991; Mutzke et al. 2019). High-density samples have small μ, and more energy is conserved between two collisions as the effect of electronic stopping is reduced.

Another effect of density is the distance between the atoms, and therefore it has an influence on the transferable energy during a collision. This energy is inversely proportional to the distance between the projectile and the center of the particle at rest. The farthest distance at which a collision occurs is the maximal impact parameter, where energy transfer is at its minimum

$$p_{\max} = \mu (2\pi)^{-1/2}. \tag{9}$$

With smaller μ, the minimum transferable energy becomes larger as the spacing between the atoms, and therefore the mean impact parameter, decreases. Higher densities therefore reduce the amount of low-energetic sputtered particles through recoils and lower the number of recoils as the energy is lost more quickly.

Mineral densities and calculated mean free paths of relevant rock-forming minerals are shown in Table 1. As an example, for enstatite ($\rho_{En} \sim 3.20$ g cm^{-3}), the default atomic model would result in

$$\begin{aligned} \rho_{En} &= \left(\frac{X_{Mg}}{\rho_{Mg}} + \frac{X_{Si}}{\rho_{Si}} + \frac{X_O}{\rho_O} \right)^{-1} \\ \rho_{En} &= \left(\frac{0.2}{0.0431} + \frac{0.2}{0.0499} + \frac{0.6}{0.0429} \right)^{-1} \text{ at A}^{-3} \\ &= 0.0442 \text{ atA}^{-3} \\ &= 1.47 \text{ gcm}^{-3}, \end{aligned} \tag{10}$$

whereas the compound model, using tabulated data for elements, results in

$$\begin{aligned} \rho_{En} &= \left(\frac{X_{MgO}}{\rho_{MgO}} + \frac{X_{SiO2}}{\rho_{SiO2}} \right)^{-1} \\ \rho_{En} &= \left(\frac{0.5}{0.1070} + \frac{0.5}{0.0797} \right)^{-1} \text{ at A}^{-3} \\ &= 0.0913 \text{ atA}^{-3} \\ &= 3.05 \text{ gcm}^{-3}. \end{aligned} \tag{11}$$

This example and the results in Table 1 demonstrate how using compound data recreates realistic mineral densities and, as a result, the mean free path within a sample well. Table 1 also shows that densities can be approximated without any manual adjustments compared to the default atomic model. Together with the hybrid binding energy model, it poses the first step in properly approximating oxides and oxide-derived minerals in Monte Carlo BCA codes such as SDTrimSP.

2.5. Fitting the Simulated Data

The modeled sputter yield by element and mass is fitted using an Eckstein fit based on the Yamamura et al. (1983) formula (Eckstein & Preuss 2003):

$$\begin{aligned} Y(\alpha) = Y(0) &\left\{ \cos\left[\left(\frac{\alpha}{\alpha_0} \frac{\pi}{2} \right)^c \right] \right\}^{-f} \\ &\times \exp\left\{ b \left(1 - 1 \Big/ \cos\left[\left(\frac{\alpha}{\alpha_0} \frac{\pi}{2} \right)^c \right] \right) \right\}, \end{aligned} \tag{12}$$

with the fitting parameters b, c, and f and the angle of incidence α. The value for α_0 is chosen as $\pi/2$ instead of being calculated by

$$\alpha_0 = \pi - \arccos \sqrt{\frac{1}{1 + E_0/E_{sp}}} \geqslant \frac{\pi}{2}, \tag{13}$$

because the projectile binding energy E_{sp} would be required or assumed, and for the typical solar wind energies E_0 in keV range with E_{sp} in the eV range, this would cause only minor deviations from $\alpha_0 = \pi/2$.

For the angular distribution of sputtered particles, the data are fitted using an adapted cosine fit function after Hofsäss & Stegmaier (2022) to take the nonsymmetrical nature of sputtered particles into account. The system of equations is as follows:

$$f(\phi) \begin{cases} A \cos^m \left(\frac{\pi}{2} \left(\frac{\pi + 2\phi}{\pi + 2\phi_{tilt}} - 1 \right) \right) & \phi \leqslant \phi_{tilt} \\ A \cos^n \left(\frac{\pi}{2} \left(1 - \frac{\pi - 2\phi}{\pi - 2\phi_{tilt}} \right) \right) & \phi \geqslant \phi_{tilt}, \end{cases} \tag{14}$$

with the scaling factor A, the tilt angle ϕ_{tilt}, the exponents m and n, and the angle ϕ.

The energy distribution data are fitted using a Thompson distribution (Thompson 1968),

$$f(E) = S \frac{E}{(E + E_0)^3}, \tag{15}$$

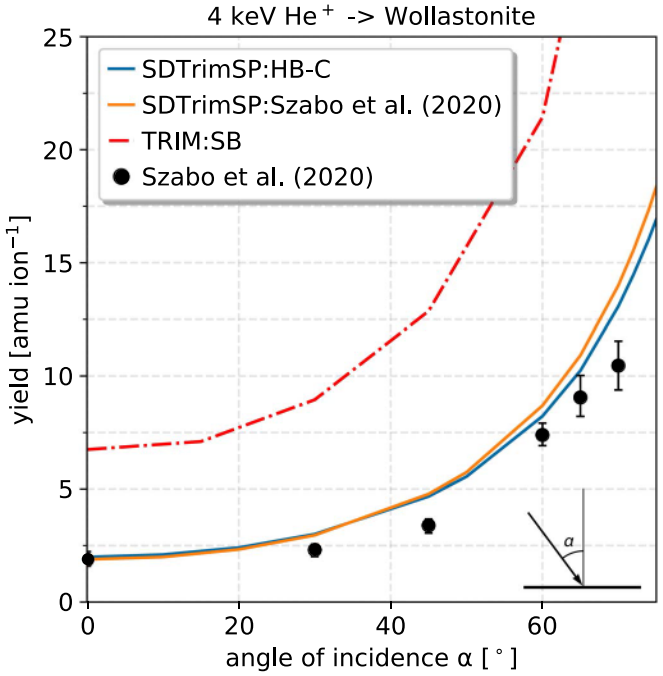

Figure 2. The agreement of the initial approach used to fit the experimental data (Szabo et al. 2020a) with the HB-C model is shown, including TRIM model results (Biersack & Eckstein 1984). The abbreviations are as follows: HB—surface binding energy (SBE) based on heat of sublimation and BBE on enthalpy of formation; C—densities calculated based on compound densities and differentiation between unbound and bound species. Szabo et al. (2020a) used an averaged SBE of all components after increasing the O_{SBE} to 6.5 eV. To reach the proper wollastonite density, they increased the O atomic density accordingly.

with a scaling factor S, the energy removed from the sputtered atom before it escapes the surface E_0 (approximately SBE, when considering a pure SB model) and the energy of the sputtered atom E. The energy peak is located at $E \approx E_0/2$.

3. Results

The validity of any new suggested model can ultimately only be verified through experimental data focusing on speciation of the sputtered material, as well as its angular and energy distribution. For now, we can only compare experimental sputter yield data in mass per impinging ion (amu/ion) and their angular distribution with model outputs. The composition of the modeled yield is stoichiometric. Lighter species are initially sputtered in an overstoichiometric way. With fluence and decreasing abundance of light species, the sputter yield composition approaches the initial sample stoichiometry, which evidently will not correspond to the sample surface composition in equilibrium. We know that the laboratory data correspond to fluences where this irradiation equilibrium is reached. For the scope of this work, we assume that the laboratory yield composition is indeed stoichiometric.

3.1. HB-C Model and Experimental Data

We first present the capabilities of the newly implemented hybrid binding energy model, which includes the compound model (HB-C). The results of the Szabo et al. (2020a) approach and the HB-C model are thereby largely identical when it comes to mass yields and recreate the experimental data reasonably well (Figure 2). The largest discrepancies lie in both the angular and energy distributions. A high SBE increases the refraction that occurs on the surface and therefore increases the spread of the angular distribution. We show this behavior in Figure 3, where the Szabo et al. (2020a) approach—with the highest SBEs of all model results shown in this work—leads to the largest tilt angle (27° at an angle of incidence of 45°) with the broadest angular distribution of all models (exponents $m = 4.9$ and $n = 1.4$ for He^+ on wollastonite). The homogeneous, atom-insensitive energy distribution of the Szabo et al. (2020a) approach is the consequence of using an identical SBE for each species (Figure 3).

3.2. All Model Comparison

In Figure 4 we compare the HB-C model with other models in relation to the experimental sputter yield data of wollastonite and enstatite. It is apparent that we find the experimental data lying between the HB-C model and the HB model. The latter thereby does not differentiate between bound and unbound species in the sample. Most relevant is that the experimental data are recreated using the HB-C model at normal incidence and close to normal incidence (<45°).

3.2.1. Angular Distributions

We compare to experimental angular distributions of Biber et al. (2022) with modeled data of enstatite in Figure 5. The largest agreement with experimental data is with the HB model, which expresses the strongest degree of forward sputtering (largest tilt angle) owing to the high binding energy of each species in the sample. The cases with lower or no BBE—this includes the unbound species within the HB-C model—clearly show a drastically reduced degree of forward sputtering compared to the HB model. Angular distribution data of TRIM are not shown, as it expresses distributions even narrower than the BB model (Figure 1 Hofsäss & Stegmaier 2022).

3.2.2. Energy Distributions

Although no experimental data exist for the irradiated enstatite, we present the modeled energy distributions of the sputter ejecta in Figure 6. The SB and SB-C models show a nearly identical energy distribution, while the HB and HB-C models express a smaller amount of low-energy particles and thus broader peaks. The more prominent, high-energy tail of sputtered particles in the HB model is due to the species experiencing large BBEs at any degree of applied fluence. In comparison, the compound model (HB-C) can build up free Mg that are consecutively sputtered without having to overcome a BBE. This in return increases the number of low-energy Mg in the energy distribution, which lies closer to the SB-C model. This is manifested in the Mg energy distribution peaking at 0.9 eV in the HB-C model compared to the 0.6 eV in the SB models and the 1.8 eV in the HB model.

4. Discussion

4.1. Sputter Yield

We were able to confirm that it is of utmost importance to properly set the density of the irradiated sample. It is evident in Figure 4 that under normal incidence the HB-C model that recreates the mineral density adequately fits the experimental data best for both H^+ and He^+ irradiation results.

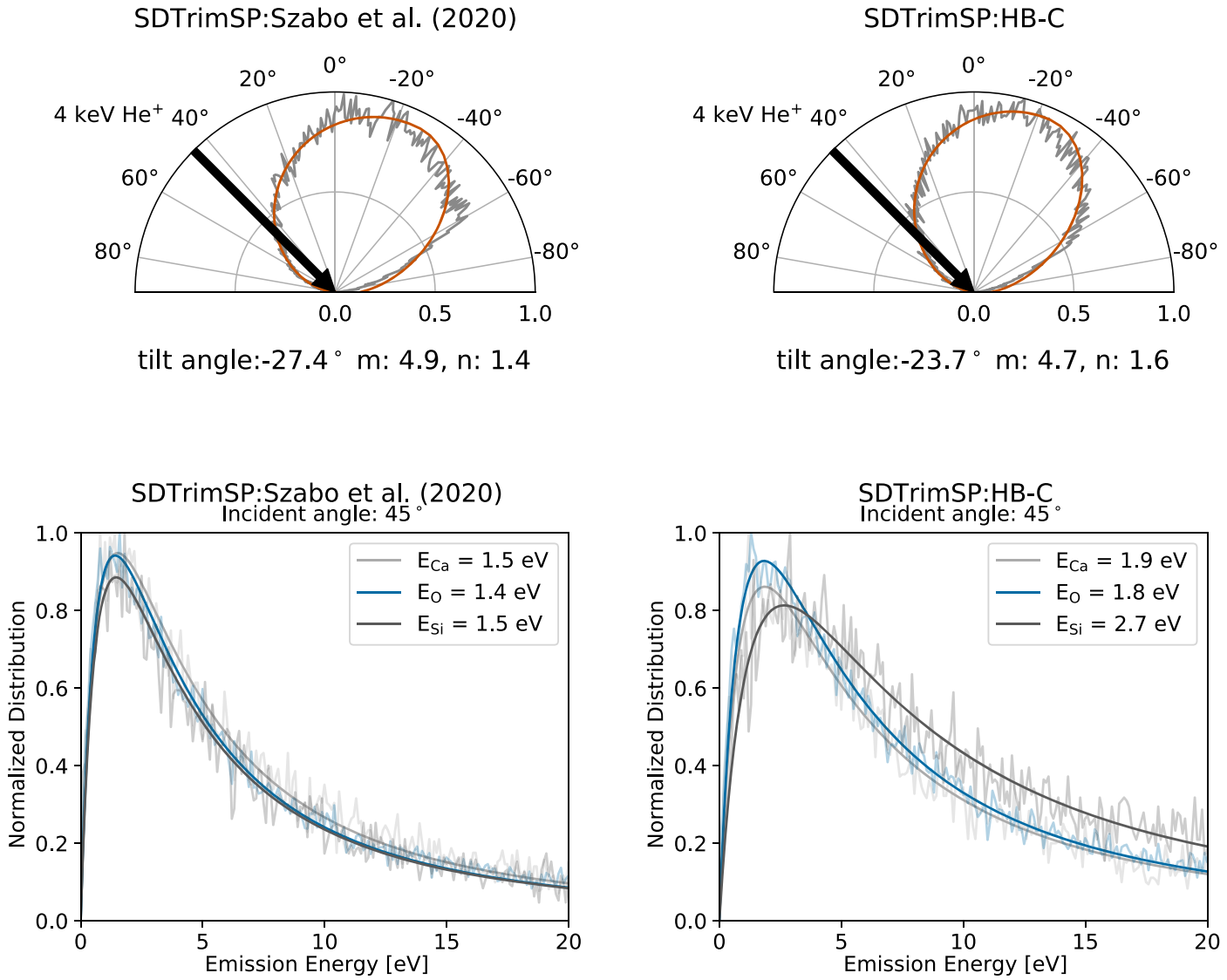

Figure 3. Modeled angular distribution of total sputter yield (data in gray, fit in orange) and energy distributions of sputter ejecta. The energy in the legend corresponds to the peak energy of the Thompson fit function, from wollastonite irradiated by 4 keV He^+. Szabo et al. (2020a) increased the O surface binding energy (SBE) to 6.5 eV, averaged SBEs for all elements, and increased O density to reach initial wollastonite density. The large surface binding energy causes a high degree of surface scattering of the ejected particles, whereas the averaging of the binding energies leads to an identical energy distribution for all species. The HB-C model uses both SBE and bulk binding energy to achieve an increase in binding energy while reliably reproducing mineral densities based on oxide compound data and differentiating between compound-bound and unbound atoms.

The experimental data of the H-irradiated wollastonite thin film express a significant deviation from SDTrimSP predictions for the flat surface sputter behavior. This could so far not be explained (Szabo et al. 2018). Nevertheless, all the experimental data in Figure 4 show good agreement with the HB-C model close to normal incidence and up to at least 45°. This is relevant for approximating irradiation of realistic, rough surfaces because yield enhancements between a flat and rough surface are generally small for incidence angles below 45° (Küstner et al. 1998; Biber et al. 2022). This is not due to impacts realistically occurring at normal incidence in nature, but due to surface roughness leading to locally reduced incidence angles for shallow impinging ions and therefore flattened mass yield distributions. This is discussed in Biber et al. (2022) for enstatite irradiation experiments and was previously shown for rough Bo and Be surfaces (Gauthier et al. 1990; Roth et al. 1991; Küstner et al. 1999).

4.2. Angular Distribution

We observed that no model can completely recreate the large polar tilt angle seen in experimental data (Figure 5). The model that comes closest is the HB model, which boasts large BBEs, subsequently leading to a rapid loss of energy with each recoil. The increased binding energy thus negatively affects the collision kinematics of long collision cascades and gives primary-knock-on collisions (i.e., Figure 2.6 in Behrisch & Wittmaack 1991) a higher significance in the angular distribution of sputtered material. More random ejecta from long collision cascades that would lead to ejecta distributions close to normal are reduced. As a consequence, the tilt of the angular distribution increases. This behavior has also been observed on binary alloys, both experimentally and through MD simulations. There, atoms sputtered from the second atomic layer form angular distributions toward the surface normal, whereas first-layer-emitted atoms have a broad

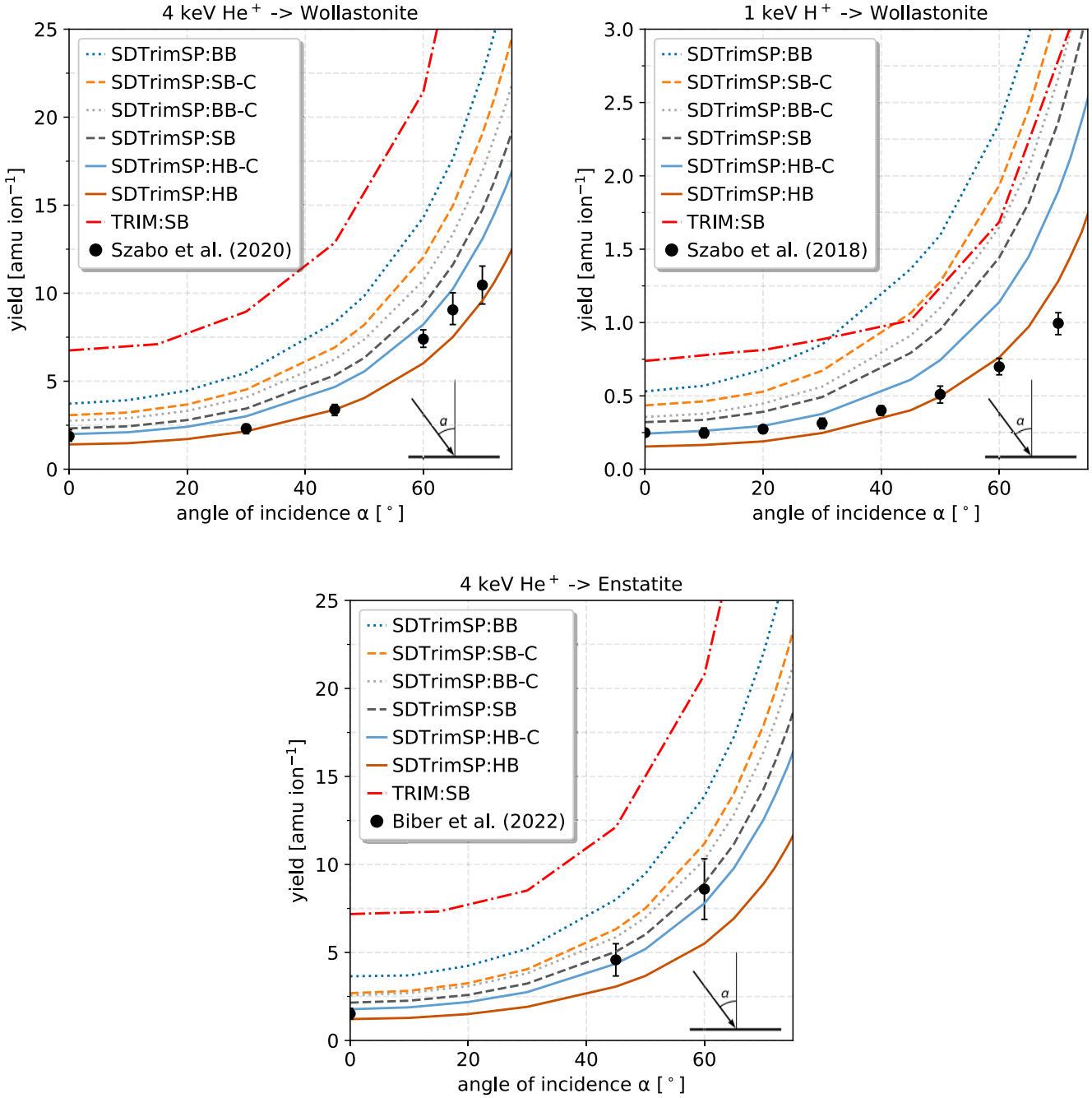

Figure 4. SDTrimSP model results compared to TRIM model results (red dashed–dotted line; Biersack & Eckstein 1984) and experimental data by Szabo et al. (2018; H^+ on wollastonite), Szabo et al. (2020a; He^+ on wollastonite) and Biber et al. (2022; He^+ on enstatite). Near-ideal mineral densities are obtained in models taking compounds (-C) into account, whereas the atomic cases represent lower densities, about a factor two below compound derived densities. Abbreviations and line styles are as follows: SB—dashed lines, tabulated enthalpy of sublimation as element surface binding energies; BB—dotted lines, tabulated enthalpy of sublimation as element bulk binding energies; HB—solid lines, tabulated enthalpy of formation as bulk binding energy and enthalpy of sublimation as surface binding energies; C—densities calculated based on compound densities and differentiation between compound-bound and unbound atoms.

distribution (Schwebel et al. 1987; Whitaker et al. 1993; Gnaser 1999). In all but the HB and HB-C models, components with low BBEs (if any) exist at the irradiation equilibrium. Energy loss within the sample is therefore less significant, which reduces the contribution of first-layer-emitted atoms and causes a near-circular plume of ejecta closer to the surface normal.

The width of the angular distribution, quantified in the cosine fit exponents (m and n; Figure 5), is also tied to the SBE. In all modeling approaches but the ones from Szabo et al. (2020a) and Hofsäss & Stegmaier (2022) the used SBEs are identical, and therefore the exponents are comparable. The BB model is narrowest (no surface potential, no refraction) and results in the lowest tilt angle with a visible forward-sputter contribution that is not able to significantly affect the tilt of the distribution. Both the HB-C model and especially the HB model lead to a larger tilt due to preventing randomly distributed, low-energy particles from leaving the surface and thus favoring forward-facing ejecta, which are observed as a peak around −60°. Toward increasing incident angles relative to the surface

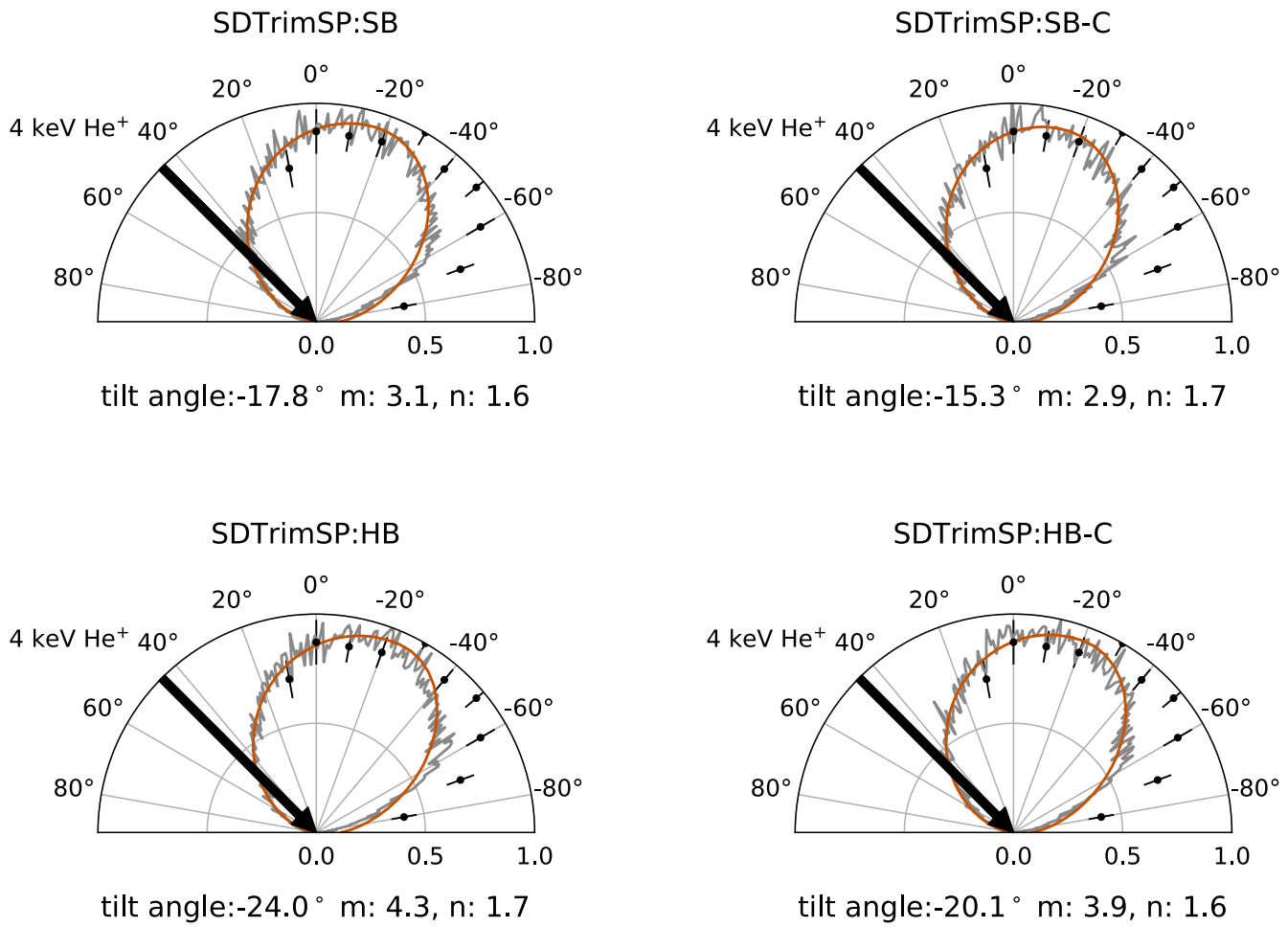

Figure 5. Polar angular distributions of total sputter yields from enstatite irradiated with 4 keV He^+ at an angle of 45° based on different model assumptions. The larger density prescribed by the compound model leads to a slightly more narrow angular distribution—seen in the smaller *m* fit exponents of 2.9 and 3.9 of the cosine fit—when compared to the atomic model *m* exponents of 3.1 and 4.3, respectively. If elements become unbound with irradiation (HB-C model), the effect of a BBE on the tilt angle is small compared to the SB model (+2.°3). If elements remain bound and experience a constant BBE and SBE (HB model), forward sputtering is more prominent (SB model tilt +6.°2). Abbreviations: SB–tabulated enthalpy of sublimation as element surface binding energies; HB—tabulated enthalpy of formation as BBE and enthalpy of sublimation as surface binding energies; C—densities calculated based on compound densities and differentiation between compound-bound and unbound atoms. Experimental data from thin-film irradiation (Biber et al. 2022) are normalized to y_{max}=1 with an error of one standard deviation.

normal (>45°, not shown), the number of single knock-on recoils increases independent of the chosen model, enhancing the peak size of the forward-aligned ejecta. Local shallow incident angles are unlikely to contribute to sputtering of a realistic, rough and/or porous sample. This is motivated by the strong sputter yield decrease observed at shallow incidence, which is related to processes of shadowing and redeposition (Küstner et al. 1999; Cupak et al. 2021; Szabo et al. 2022a; Biber et al. 2022). For this reason, the forward-facing peak at shallow incidence angles is not expected to be present for sputtering of regolith. Furthermore, the contribution to the total sputtered particles is negligible for nonshallow incident angles.

The sample roughness could in theory be another cause for the discrepancy between model and experimental data. The surface of the enstatite glassy thin film was analyzed using an atomic force microscope, and its roughness was deemed negligible (Biber et al. 2022). Furthermore, when compared to the angular distribution of a rougher surface, the thin-film angular distribution is nearly identical when normalized (Figures 2 and 3 in Biber et al. 2022). Roughness is therefore unlikely to account for the discrepancy seen in Figure 5.

4.3. Energy Distribution

Energy distributions of particles from SB models follow Thompson distributions with peak energies close to 1/2 of the SBEs used. The HB model, however, reaches peak energies that are approximately equal to the SBEs used (E_s(Mg) = 1.5, E_s(O) = 2.6, and E_s(Si) = 4.7), and the HB-C model shows elevated energies that are closer to SBE/2. At constant SBEs, the peaks of the energy distribution are widened with increasing BBEs (Figure 6). Models that include a BBE experience a shift toward larger energies with a broadening of the energy distribution, as low-energy particles are not reflected back into the sample. This behavior follows the O_2-covered metal irradiation experiments performed by Dullni (1984), Wucher & Oechsner (1986), and Wucher & Oechsner (1988). Therefore, the peak energies of the energy distributions, fitted by Thompson distributions, do not correspond to the enthalpy of sublimation ΔH_s of the atomic species, but rather the combination of enthalpy of formation ΔH_f of the oxide present with ΔH_s (Figure 3 in Dullni 1984). The expected energy distribution broadening in a system where O_2 is present is thus recreated by both the HB and HB-C models with the same

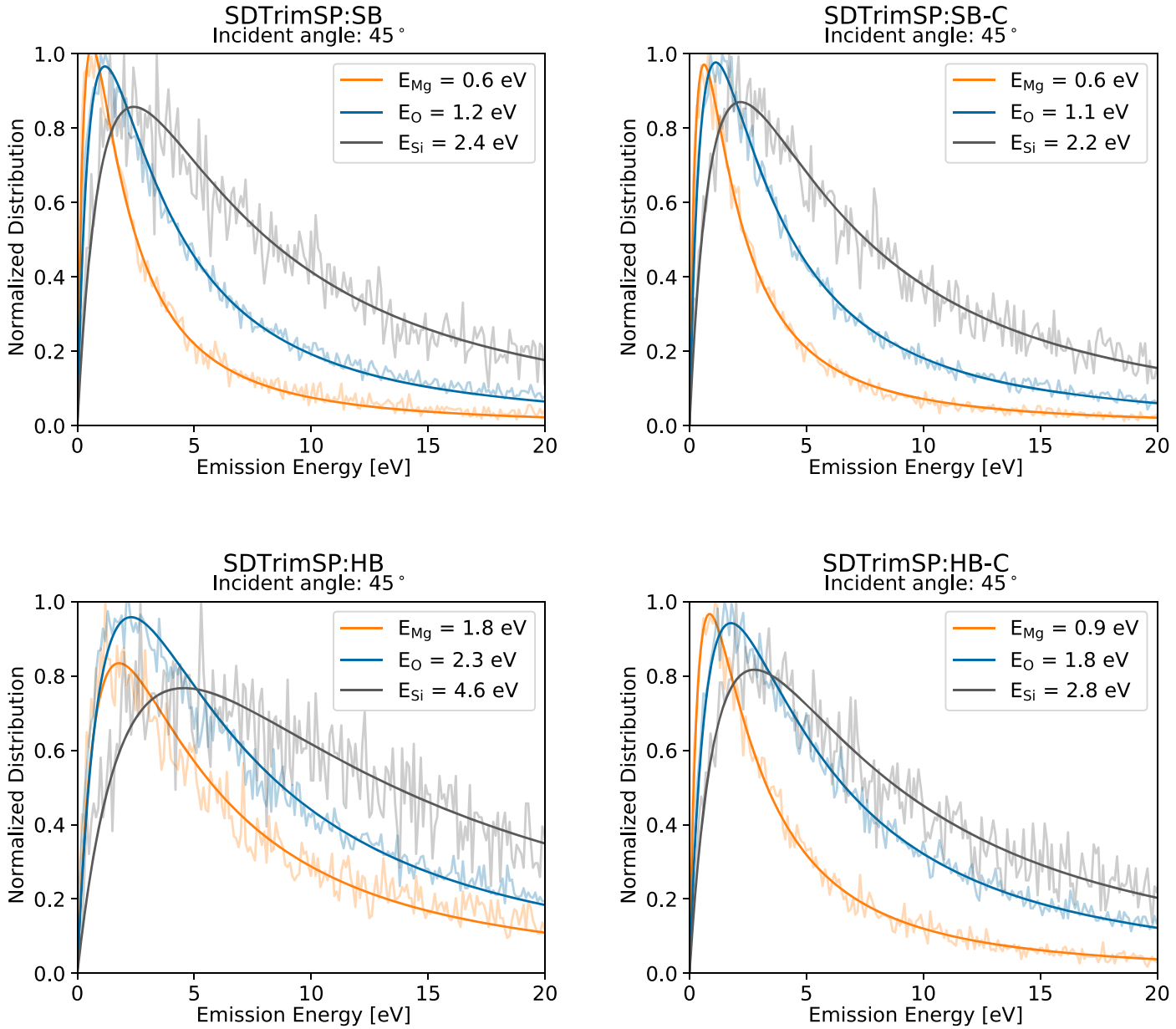

Figure 6. Energy distributions of sputtered elements from enstatite irradiated with 4 keV He^+ at an angle of 45° based on different model assumptions. The energy in the legend corresponds to the peak energy of the Thompson fit function. Abbreviations: SBE—tabulated enthalpy of sublimation as element SBEs; HB—tabulated enthalpy of formation as BBE and enthalpy of sublimation as SBEs; C—densities calculated based on compound densities and differentiation between compound-bound and unbound atoms.

underlying assumptions, making it a valuable addition to the SB and BB models, which, on the contrary, cannot recreate the broadening. The results are also reminiscent of the broadening observed by increasing SBEs as in Morrissey et al. (2022), and the conclusion is the same. Larger total binding energies lead to a larger high-energy fraction of the sputtered particles while reducing the number of ejected particles. In exospheres around solar-wind-exposed surfaces, less abundant but more energetic particles would then be detectable farther from the surface.

4.3.1. Inclusion of Intermediary Compounds

It becomes evident from Figure 6 that larger peak energies can be achieved if the atomic species remain in a bound condition. In the scope of this work we did not explore the formation of possible intermediates. The current implementation will always break up the compound, and one of the products will continue to travel through the sample. If there are enough free elements available, only the original oxide can form, and therefore the model—for the example of SiO_2—is limited to

$$SiO_2 \rightleftharpoons Si + O + O. \quad (16)$$

A more sophisticated model would need to include the following reactions:

$$SiO_2 \rightleftharpoons Si + O_2 \quad (17)$$

$$SiO_2 \rightleftharpoons SiO + O \quad (18)$$

$$SiO \rightleftharpoons Si + O \quad (19)$$

$$O_2 \rightleftharpoons O + O \quad (20)$$

$$Si_2 \rightleftharpoons Si + Si, \quad (21)$$

Table 3
Effect of an Increased Sodium Surface Binding Energy on Total Yield and Angular Distribution from Simulating 1 keV H^+ Irradiation on Albite ($NaAlSi_3O_8$)

	E_s(Na) (eV)	Y_{Na} ($10^{-3}\frac{at}{ion}$)	$\phi_{tilt}(45°)$ (deg)	m, n (unit of unity)
M22[a]	7.9	0.41	…	…
SB	7.9	0.79	34.4	5.1, 1.5
SB	1.1	1.08	16.1	3.0, 2.0
HB-C	1.1	1.10	18.9	3.9, 2.3

Notes.
[a] Computed in static mode; Y_{Na}—sodium sputter yield; E_s(Na)—SBE of sodium; $\phi_{tilt}(45°)$—angular distribution tilt angle at an ion incidence angle of 45° relative to surface normal; m, n—cosine fit exponents.
References. M22: Morrissey et al. (2022).

which would reduce the number of unbound atoms in the sample. The resulting energy distribution would thus lie closer to the hybrid model (HB), where atomic species are considered to remain bound in their compounds. To fully simulate the process of amorphization, we would need to know what drives the stability of the different products within a mineral in irradiation equilibrium.

4.4. Effect of Increased SBE

To demonstrate the effect of an increased SBE, we compared the standard SB model and the newly implemented HB-C model with the results of Morrissey et al. (2022). As of now, there are only SBEs available for Na in Na silicates with increasing coordination numbers (number of O atoms being a neighbor to Na). Therefore, we only compare the results for albite $NaAlSi_3O_8$ irradiated by 1 keV H^+ (Table 3). For a static computation in SDTRimSP of albite with increased Na binding energies of $E_s(Na) = 7.9$ eV Morrissey reported a yield of 4.12×10^{-4} Na/ion at normal incidence. If SDTrimSP is run in dynamic mode, the yield at the irradiation equilibrium is increased by a factor of two, to 7.90×10^{-4} Na/ion. If compared to the yields of the SB model (1.08×10^{-3} Na/ion) and the HB-C model (1.10×10^{-3}), the dynamic Na yields with $E_s(Na) = 7.9$ eV differ by 30%. This similarity in SB and HB-C equilibrium yield is due to free Na atoms in the HB-C model behaving identically to the Na in the BB model. Na_2O having the lowest enthalpy of formation and therefore bound Na in the HB-C model is not prioritized in forming bonds with free O, causing an accumulation of Na in the surface layer at irradiation equilibrium as a result. The increase in density and BBE that is imbued in the HB-C model therefore does not apply to Na at the irradiation equilibrium, as no surface Na_2O exists. The energy peak of the Morrissey approach ($E_s(Na) = 7.9$ eV) is, as expected, around 4 eV (approx. $SBE/2 = 7.8/2$) with the tilt angle exceeding the results of both the SB and HB-C models by a factor of two and expressing a wide distribution as given by the large fit exponents (m and n). In conclusion, the effect of increasing the SBE of Na is apparent not only in actual yields (−30%) but also in the angular and energy energy distributions.

4.5. Experiments Needed for Evaluation

Both the angular and energy distribution data of sputtered minerals depend on the chosen surface and BBEs. Extensive experiments to properly discriminate between different sputtered species, as well as obtaining the species' energy distribution, would be highly valuable for constraining surface and BBEs. Obtaining energy distributions would give a needed insight on the energy peak broadening effect occurring on minerals. If this was available, further restrictions on realistic binding energies could be enforced, whereas SBEs define the energy peak position and width and BBEs act as a "broadening agent" for further enhancing energy peak widths. As a side effect, the increasing and/or shifting of binding energies between SBE and BBE could achieve the desired forward tilt of the sputtered material while not degrading the agreement in total mass yields.

It would be pleasing, although unlikely, if experimental data of energy and angular distributions could be recreated based on solely tabulated thermodynamic data. Nevertheless, we expect SBEs to be larger than tabulated, as demonstrated for an ideal, intact crystal lattice in MD by Morrissey et al. (2022). Using one single SBE might not be appropriate to describe an altered sample, however. SBEs at various degrees of alteration would be necessary to understand the evolution of the SBE with increasing levels of amorphization. The correlation of SBE with coordination number shown by Morrissey is reminiscent of the SBE dependence on the degree of amorphization, and a similar behavior is expected for the surfaces of irradiated samples (Loeffler et al. 2009; Biber et al. 2022). One should, however, refrain from adjusting the SBE like a fit parameter to best reproduce experimental data. For now we propose the use of the HB-C model for recreating experimental mass changes, with the enthalpy of sublimation as SBE and the enthalpy of formation of the mineral-forming compounds as BBE.

5. Conclusions

We introduced a hybrid binding energy model in the BCA code SDTrimSP with an underlying compound model that combines tabulated data for SBEs, BBEs, and densities for mineral samples while differentiating between free and compound-bound components. With regard to previous modeling approaches, we offer an alternative that minimizes the number of free parameters further and well reproduces experimental data. The new compound hybrid model (HB-C) merges the pure SB and BB models while reproducing mineral properties. This includes proper mineral densities through tabulated compound data, but also combining surface and BBEs, which leads to increased energy loss within the collision cascade, causing energy peak broadening as expected in a O-dominated system (e.g., Dullni 1984).

Although the differences between the SB model and the HB-C model seem minor, the model infrastructure allows for further inclusions that are reasonable in terms of mineralogy and physics. Furthermore, comparisons with experimental sputter yields result in unprecedented agreement between 0° (normal incidence) and 45°, a range that is especially of interest for modelers that require sputter yields as inputs. The HB-C model thus convinces on the following points: (1) good agreement with existing experimental data in parameter spaces relevant to exosphere modelers; (2) corrects for underestimation of the default sample density computation based on atomic densities by using tabulated densities of compounds instead; (3) sets SBEs and BBEs based on tabulated enthalpy of sublimation and enthalpy of formation of compounds, respectively, which allows for a universal application to

minerals; (4) does not require setting parameters such as SBE, BBE, density, and cutoff energy (SB model four, isbv = 4, in SDTrimSP), therefore greatly increasing the ease of use. For the time being, the HB-C model does an exemplary job in recreating experimental sputter data while producing reasonable energy and angular distributions of ejecta.

Financial support has been provided by the Swiss National Science Foundation Fund (200021L_182771/1), the Austrian Science Fund FWF (project No. I 4101-N36), and KKKÖ (Commission for the Coordination of Fusion research in Austria at the Austrian Academy of Sciences ÖAW). The authors gratefully acknowledge support from NASA's solar system Exploration Research Virtual Institute (SSERVI) via the LEADER team, grant No. 80NSSC20M0060.

Software: SDTrimSP (Mutzke et al. 2019), TRIM (in SRIM package) (Biersack & Eckstein 1984; Ziegler et al. 2010).

Appendix
Averaging the Surface Binding Energies

If we assume, like in Szabo et al. (2020a), that the binding energy that has to be overcome is solely dependent on the number of bonds with O, called the coordination number, the SBE of any component would be a function of the O content in the sample. A way to simulate this effect of the coordination number of atoms is to assume an averaged binding energy, which is a mass balance over all species present in the compound. In SDTrimSP, this is implemented as the SB model two (isbv = 2, Mutzke et al. 2019):

$$\mathrm{SBE} = \sum q_i Es_i, \tag{A1}$$

where q_i is the concentration and Es_i is the SBE of component i. This results in a single SBE for all components and therefore the compound. This was applied in Szabo et al. (2020a) in addition to the density correction to best fit wollastonite ($CaSiO_3$) data. To illustrate this effect, let us assume an increased Es_O of 6.5 eV (Szabo et al. 2020a) and compare it to the default Es_O of 2.58247 eV. For nepheline, ($NaAlSiO_4$) this would result in an average Es of 5.03 eV for all species instead of 2.79 eV with

$$\begin{aligned} q_{\mathrm{Na}} &= q_{\mathrm{Al}} = q_{\mathrm{Si}} = 1/7 \\ q_{\mathrm{O}} &= 4/7 \\ Es_{\mathrm{Na}} &= 1.11\ \mathrm{eV} \\ Es_{\mathrm{Al}} &= 3.41\ \mathrm{eV} \\ Es_{\mathrm{Si}} &= 4.66\ \mathrm{eV} \\ Es_{\mathrm{O}} &= 2.58\ \mathrm{eV} \Rightarrow Es_{\mathrm{avg}} = 2.79\ \mathrm{eV} \\ Es_{\mathrm{O}} &= 6.50\ \mathrm{eV} \Rightarrow Es_{\mathrm{avg}} = 5.03\ \mathrm{eV}. \end{aligned} \tag{A2}$$

On first glance, this seems to work, as the suggested SBE for Na in a pristine, crystalline mineral is about 4.8 eV based on MD simulations (Morrissey et al. 2022). In the case of the major rock-forming mineral albite ($NaAlSi_2O_6$; $Es_{Na} = 8.4$ eV; Morrissey et al. 2022), the isbv = 2 approximation with $Es_O = 6.5$ eV nets an average SBE of 5.4 eV, which does not reproduce the high binding energies of Na suggested by MD. This suggests that adjusting SBEs based on a single component has its limits when it comes to simulating bond strengths of complex mineral structures.

ORCID iDs

Noah Jäggi https://orcid.org/0000-0002-2740-7965
Herbert Biber https://orcid.org/0000-0002-9854-2056
Johannes Brötzner https://orcid.org/0000-0001-9999-9528
Paul Stefan Szabo https://orcid.org/0000-0002-7478-7999
Friedrich Aumayr https://orcid.org/0000-0002-9788-0934
Peter Wurz https://orcid.org/0000-0002-2603-1169
André Galli https://orcid.org/0000-0003-2425-3793

References

Arredondo, R., Oberkofler, M., Schwarz-Selinger, T., et al. 2019, Nuclear Materials and Energy, 18, 72
Baker, D. N., Poh, G., Odstrcil, D., et al. 2013, JGRA, 118, 45
Baretzky, B., Möller, W., & Taglauer, E. 1992, Vacuu, 43, 1207
Behrisch, R., & Eckstein, W. 2007, Sputtering by Particle Bombardment: Experiments and Computer Calculations from Threshold to MeV Energies (Berlin: Springer), 507
Behrisch, R., & Wittmaack, K. 1991, Sputtering by Particle Bombardment III: Characteristics of Sputtered Particles (Berlin: Springer)
Benkhoff, J., van Casteren, J., Hayakawa, H., et al. 2010, P&SS, 58, 2
Benninghoven, A., Rudenauer, F. G., & Werner, H. W. 1987, Secondary Ion Mass Spectrometry: Basic Concepts, Instrumental Aspects, Applications and Trends (New York: Wiley)
Betz, G. 1987, NIMPB, 27, 104
Betz, G., & Wien, K. 1994, IJMSI, 140, 1
Biber, H., Brötzner, J., Jäggi, N., et al. 2022, PSJ, 3, 271
Biersack, J., & Haggmark, L. 1980, NucIM, 174, 257
Biersack, J. P., & Eckstein, W. 1984, ApPhy, 34, 73
Cassidy, T. A., Merkel, A. W., Burger, M. H., et al. 2015, Icar, 248, 547
Cupak, C., Szabo, P. S., Biber, H., et al. 2021, ApSS, 570, 151204
Deer, W. A., Howie, R. A., & Zussman, J. 1992, An Introduction to the Rock-forming Minerals (2nd ed.; Harlow: Longman Scientific & Technical)
Domingue, D. L., Chapman, C. R., Killen, R. M., et al. 2014, SSRv, 181, 121
Dukes, C., & Baragiola, R. 2015, Icar, 255, 51
Dukes, C. A., Chang, W. Y., Famá, M., & Baragiola, R. A. 2011, Icar, 212, 463
Dullni, E. 1984, NIMPB, 2, 610
Eckstein, W. 1991, Computer Simulation of Ion-solid Interactions, Vol. 10 (Berlin: Springer)
Eckstein, W., & Preuss, R. 2003, JNuM, 320, 209
Elphic, R. C., Delory, G. T., Hine, B. P., et al. 2014, SSRv, 185, 3
Fatemi, S., Poppe, A., & Barabash, S. 2020, JGRA, 125, e2019JA027706
Gades, H., & Urbassek, H. M. 1992, NIMPB, 69, 232
Gamborino, D., & Wurz, P. 2018, P&SS, 159, 97
Gauthier, E., Eckstein, W., László, J., & Roth, J. 1990, JNuM, 176, 438
Gershman, D. J., Zurbuchen, T. H., Fisk, L. A., et al. 2012, JGRA, 117, A00M02
Glass, A. N., Raines, J. M., Jia, X., et al. 2022, JGRA, 127, e2022JA030969
Gnaser, H. 1999, Low-energy Ion Irradiation of Solid Surfaces, Vol. 146 (Berlin: Springer), 41
Grava, C., Killen, R. M., Benna, M., et al. 2021, SSRv, 217, 1
Hijazi, H., Bannister, M. E., Meyer, H. M., Rouleau, C. M., & Meyer, F. W. 2017, JGRE, 122, 1597
Hobler, G. 2013, NIMPB, 303, 165
Hofsäss, H., & Stegmaier, A. 2022, NIMPB, 517, 49
Jackson, D. P. 1975, CaJPh, 53, 1513
Janches, D., Berezhnoy, A. A., Christou, A. A., et al. 2021, SSRv, 217, 50
Kazakov, A., Milillo, A., Lazzarotto, F., et al. 2022, EPSC, 16, EPSC2022–810
Ken Knight, C. E., & Wehner, G. K. 1967, Investigation of Sputtering Effects on the Moon's Surface, 3107 NASA, https://ntrs.nasa.gov/citations/19670028248
Killen, R. M., Morrissey, L. S., Burger, M. H., et al. 2022, PSJ, 3, 139
Küstner, M., Eckstein, W., Dose, V., & Roth, J. 1998, NIMPB, 145, 320
Küstner, M., Eckstein, W., Hechtl, E., & Roth, J. 1999, JNuM, 265, 22
Lindhard, J., & Scharff, M. 1961, PhRv, 124, 128
Loeffler, M. J., Dukes, C. A., & Baragiola, R. A. 2009, JGR, 114, E03003
Lue, C., Futaana, Y., Barabash, S., et al. 2011, GeoRL, 38, 3202
Madey, T. E., Johnson, R. E., & Orlando, T. M. 2002, SurSc, 500, 838
Mangano, V., Milillo, A., Mura, A., et al. 2007, P&SS, 55, 1541
Martinez, R., Langlinay, T., Ponciano, C. R., et al. 2017, NIMPB, 406, 523
McNutt, R. L., Jr., Benkhoff, J., Fujimoto, M., & Anderson, B. J. 2018, in Mercury: The View after MESSENGER, ed. S. C. Solomon, L. R. Nittler, & B. J. Anderson (Cambridge: Cambridge Univ. Press), 544

Milillo, A., Fujimoto, M., Murakami, G., et al. 2020, SSRv, 216, 93
Möller, W., & Eckstein, W. 1984, NIMPB, 2, 814
Möller, W., & Posselt, M. 2001, TRIDYN FZR User Manual, Technical Rep., FZR 317, Dresden: Forschungszentrum Rossendorf
Morrissey, L. S., Tucker, O. J., Killen, R. M., Nakhla, S., & Savin, D. W. 2022, ApJL, 925, L6
Mura, A., Wurz, P., Lichtenegger, H. I. M., et al. 2009, Icar, 200, 1
Mutzke, A., Schneider, R., Eckstein, W., et al. 2019, SDTrimSP v6.00, Max-Planck-Institut für Plasmaphysik
Nénon, Q., & Poppe, A. R. 2020, PSJ, 1, 69
Orsini, S., Livi, S., Lichtenegger, H., et al. 2021, SSRv, 217, 11
Paige, D. A., Foote, M. C., Greenhagen, B. T., et al. 2010, SSRv, 150, 125
Pfleger, M., Lichtenegger, H., Wurz, P., et al. 2015, P&SS, 115, 90
Poppe, A., Farrell, W., & Halekas, J. S. 2018, JGRE, 123, 37
Raines, J. M., Dewey, R. M., Staudacher, N. M., et al. 2022, JGRA, 127, e2022JA030397
Roth, J., Bohdansky, J., & Eckstein, W. 1983, NIMPR, 218, 751
Roth, J., Bohdansky, J., & Ottenberger, W. 1979, Data on low energy light ion sputteringIPP 9/26Max-Planck-Institut für Plasmaphysik, 98
Roth, J., Eckstein, W., Gauthier, E., & Laszlo, J. 1991, JNuM, 179, 34
Samartsev, A. V., & Wucher, A. 2006, ApSS, 252, 6470
Schaible, M. J., Dukes, C. A., Hutcherson, A. C., et al. 2017, JGRE, 122, 1968
Schaible, M. J., Sarantos, M., Anzures, B. A., Parman, S. W., & Orlando, T. M. 2020, JGRE, 125, e2020JE006479
Schwebel, C., Pellet, C., & Gautherin, G. 1987, NIMPB, 18, 525
Sigmund, P. 1969, PhRv, 184, 383
Solomon, S. C., McNutt, R. L., Gold, R. E., et al. 2001, P&SS, 49, 1445
Suzuki, Y., Yoshioka, K., Murakami, G., & Yoshikawa, I. 2020, JGRE, 125, e2020JE006472
Szabo, P. S., Biber, H., Jäggi, N., et al. 2020a, ApJ, 891, 100
Szabo, P. S., Biber, H., Jäggi, N., et al. 2020b, JGRE, 125, e2020JE006583
Szabo, P. S., Chiba, R., Biber, H., et al. 2018, Icar, 314, 98
Szabo, P. S., Cupak, C., Biber, H., et al. 2022a, Surfaces and Interfaces, 30, 101924
Szabo, P. S., Poppe, A. R., Biber, H., et al. 2022b, GeoRL, 49, e2022GL101232
Szymoński, M. 1981, PhLA, 82, 203
Thompson, M. W. 1968, PMag, 18, 377
Van der Heide, P. 2014, Secondary Ion Mass Spectrometry: An Introduction to Principles and Practices (New York: Wiley)
Vorburger, A., Wurz, P., Barabash, S., et al. 2013, JGRA, 118, 3937
Whitaker, T. J., Jones, P. L., Li, A., & Watts, R. O. 1993, RScI, 64, 452
Winslow, R. M., Anderson, B. J., Johnson, C. L., et al. 2013, JGRA, 118, 2213
Wucher, A., & Oechsner, H. 1986, NIMPB, 18, 458
Wucher, A., & Oechsner, H. 1988, SurSc, 199, 567
Wurz, P. 2005, in ESA TSP-600, The Dynamic Sun: Challenges for Theory and Observations, 11th European Solar Physics Meeting
Wurz, P., Fatemi, S., Galli, A., et al. 2022, SSRv, 218, 1
Wurz, P., Rohner, U., Whitby, J. A., et al. 2007, Icar, 191, 486
Wurz, P., Whitby, J. A., Rohner, U., et al. 2010, P&SS, 58, 1599
Yamamura, Y., Itikawa, Y., & Itoh, N. 1983, Angular Dependence of Sputtering Yields of Monatomic Solids (Nagoya: Nagoya Univ.)
Ziegler, J. F., & Biersack, J. P. 1985, in Treatise on Heavy-Ion Science, ed. D. A. Bromley (New York: Springer), 93
Ziegler, J. F., Ziegler, M. D., & Biersack, J. P. 2010, NIMPB, 268, 1818